

Spatial heterogeneity of axon induces complex dynamics of enhanced conduction failure rate and irregular pattern of action potentials

Xinjing Zhang(张新景), Yuye Li(李玉叶), Linan Guan(关利南), and Huaguang Gu(古华光)
Citation: Chin. Phys. B, 2026, 35 (**6**): 068704. DOI: 10.1088/1674-1056/ae311c
http://cpb.iphy.ac.cn; http://iopscience.iop.org/cpb

What follows is a list of articles you may be interested in

Coupling-diversity-enhanced weak signal propagation in bistable networks

Yashi Zhang(章雅诗), Shanshan Cheng(程姗姗), Jie Fu(扶杰), and Lulu Lu(鹿露露)
Chin. Phys. B, 2026, 35 (**4**): 048704. DOI: 10.1088/1674-1056/ae23a9

Frequency-tunable spiking dynamics of Chua corsage memristors

Qijian Wu(吴奇键), Peipei Jin(靳培培), Xiameng Wu(吴夏萌), Meiyuan Gu(顾梅园), Wei Zhou(周玮), Yujiao Dong(董玉姣), Yan Liang(梁燕), and Long Chen(陈龙)
Chin. Phys. B, 2026, 35 (**4**): 048703. DOI: 10.1088/1674-1056/ae3c95

Patterned line-illumination mesoscopy with a moving slit for enhancing background suppression in cortex-wide mouse brain imaging

Chaowei Zhuang(庄超玮), Yi Yang(杨懿), and Hao Xie(谢浩)
Chin. Phys. B, 2026, 35 (**2**): 028704. DOI: 10.1088/1674-1056/adf4a6

Simulation of the physical process of neural electromagnetic signal generation based on a simple but functional bionic Na^+ channel

Fan Wang(王帆), Jingjing Xu(徐晶晶), Yanbin Ge(葛彦斌), Shengyong Xu(许胜勇),Yanjun Fu(付琰军), Caiyu Shi(石蔡语), and Jianming Xue(薛建明)
Chin. Phys. B, 2022, 31 (**6**): 068701. DOI: 10.1088/1674-1056/ac3cac

An electromagnetic view of relay time in propagation of neural signals

Jing-Jing Xu(徐晶晶), San-Jin Xu(徐三津), Fan Wang(王帆), and Sheng-Yong Xu(许胜勇)
Chin. Phys. B, 2021, 30 (**2**): 028701. DOI: 10.1088/1674-1056/abc0d2

SPECIAL TOPIC — Biophysical circuits: Modeling & applications in neuroscience

Spatial heterogeneity of axon induces complex dynamics of enhanced conduction failure rate and irregular pattern of action potentials

Xinjing Zhang(张新景)[1], Yuye Li(李玉叶)[2,†], Linan Guan(关利南)[1], and Huaguang Gu(古华光)[3]

[1] *School of Mathematics and Statistics, North China University of Water Resources and Electric Power, Zhengzhou* 450045, *China*
[2] *College of Mathematics and Computer Science, Chifeng University, Chifeng* 024000, *China*
[3] *School of Aerospace Engineering and Applied Mechanics, Tongji University, Shanghai* 200092, *China*

(Received 23 October 2025; revised manuscript received 19 December 2025; accepted manuscript online 25 December 2025)

Many recent experiments present a novel phenomenon in which some action potentials/spikes fail to conduct along thin axons, a phenomenon named conduction failure, differing from the common view of faithful conduction. For instance, the failure rate of spikes increases along the conduction distance, and irregular firing patterns appear in C-nerve fibers related to pathological pain. However, in the frequently used theoretical model of axons, which contains homogeneous compartments with electrical coupling, only regular firing patterns and unchanged failure rates are simulated. In the present paper, an axonal model containing compartments with heterogeneous potassium conductance is considered. First, the spatial heterogeneity induces irregular firing and an enhanced conduction failure rate of spikes at the compartments with large potassium conductance, closely matching experimental observations. Second, the regularities of the failure are analyzed. Larger heterogeneity induces more compartments with enhanced failure rates. High frequency of action potentials, weak coupling currents, and high potassium conductance induce high failure rates. Finally, the current threshold to evoke an action potential from the damping afterpotential related to Hopf bifurcation is obtained, providing explanations for conduction failure. For compartments with large potassium conductance, the membrane potential, coupling current, and total ionic current are low, resulting in a high threshold and an enhanced failure rate. The results provide explanations for the complex dynamics of conduction failure in the C-fiber and suggest measures to modulate pathological pain.

Keywords: conduction failure, bifurcation and threshold, spatial heterogeneity, irregular firing pattern

PACS: 87.19.lb, 87.19.lq, 87.19.rp

DOI: 10.1088/1674-1056/ae311c **CSTR:** 32038.14.CPB.ae311c

1. Introduction

In the nervous system, nonlinear and spatiotemporal behaviors play very crucial roles in brain functions and diseases.[1–3] It is well established that action potentials/spikes are related to the dynamics of ionic channels such as potassium and sodium channels, which are described by the Hodgkin–Huxley (HH) model.[4] In nonlinear dynamics, action potentials originate from bifurcations and/or responses to stimulation with suitable frequency and amplitude. The conduction of action potentials along axons exhibits spatiotemporal dynamics, such as wave propagation, playing a role in transmitting information mediated by action potentials from one neuron to another.[5–10] In addition to ionic channels, the conduction dynamics of spikes are also modulated by the topology of axons, which determines the conduction speed and capacity. For an axon with a large radius, such as the A_δ-fiber (myelinated fiber), each action potential can propagate rapidly, which has been widely accepted.[6,10,11] However, in an increasing number of experiments on axons with small radii, such as the C-fiber (unmyelinated fiber), some spikes fail to propagate to the other end, a phenomenon known as conduction failure.[12–15] Recently, myelinated fibers have also been identified to exhibit conduction failure.[16,17] Conduction failure has been related to multiple functions such as muscle contraction coordination, peripheral-to-central signal conversion, and memory decision-making, as well as diseases such as diabetic hyperalgesia,[13–15] epilepsy,[18] and multiple sclerosis.[19–21] Therefore, identifying the nonlinear and spatiotemporal dynamics of conduction failure is a very important issue.

In theory, the propagation of spikes along C-fibers is described by a partial differential equation, such as the reaction–diffusion equation of the HH model.[22–24] For convenience, the propagation of action potentials can be described by a chain network containing compartments/nodes of the HH model with electrical coupling.[25–27] The propagation dynamics are mainly determined by three factors, as well as other factors such as temperature[17,28,29] and noise.[30] The three main factors are the diffusion/coupling current related to the axonal radius, the dynamics of a node modulated by ionic channels, and the frequency of action potentials induced by stimulation at one end of the axon. These three factors have been widely studied experimentally. For instance, for a C-

†Corresponding author. E-mail: liyuye2000@163.com

© 2026 Chinese Physical Society and IOP Publishing Ltd. All rights, including for text and data mining, AI training, and similar technologies, are reserved.

fiber with a small radius, a small coupling strength (g_c) results in a weak coupling current. Consequently, a high conduction failure rate was observed in the C-fibers of diabetic rats,[14,15] which is related to pathological pain. Downregulated expression of potassium (K^+) channels can reduce the conduction failure rate of spikes and is therefore suggested as a means to alleviate pain.[13–15] Conversely, upregulated expression of K^+ channels can suppress pain. For the third factor, a high spike frequency induced by pathological factors or high-frequency stimulation (small period (T_s)) can enhance the conduction failure rate.[31,32]

In theoretical studies,[26,27,33,34] it has also been confirmed that smaller coupling strengths (g_c) and higher stimulation frequencies ($1/T_s$) induce higher conduction failure rates. Furthermore, decreasing K^+ conductance reduces the conduction failure rate. These results are explained by bifurcation analysis and the current threshold required to evoke a spike from a damping afterpotential associated with a Hopf bifurcation.[27] Despite these advances, two important experimental phenomena related to conduction failure have not been well explained. One is the irregular firing pattern, and the other is the increasing conduction failure rate with conduction distance.[12] Two typical firing patterns associated with conduction failure were observed. One is intermittent conduction failure, exhibiting an on–off firing pattern, i.e., a train of action potentials conducts while another train fails to conduct. The other is that action potentials randomly fail to conduct, resulting in an irregular or stochastic firing pattern.[12] In theoretical models without stochastic factors, only a regular firing pattern is reproduced, and the conduction failure rate remains unchanged with conduction distance.[26,27,34] When white noise is considered, the on–off pattern can be explained.[24] However, the irregular firing pattern associated with random conduction failure has not yet been reproduced and explained. Therefore, revealing the mechanism underlying the irregular firing pattern, as well as the increase in the conduction failure rate with conduction distance, is a key issue for understanding conduction dynamics. Recently, heterogeneous distributions of ion channels along axons have been considered in studies of action potential propagation,[35–45] for example, in marine invertebrates,[42] rodents,[43,44] and even humans.[45] The heterogeneity of ion channels affects the efficiency of action potential conduction.[46] Therefore, considering the heterogeneity of ion conductance along axons may provide a way to understand the irregular firing pattern associated with random conduction failure.

In this paper, to address the two questions related to K^+ channels, the spatial heterogeneity of K^+ channels along an axon is considered in a chain-network model. Irregular firing patterns associated with random conduction failure and the increasing conduction failure rate with conduction distance are then reproduced,[12] demonstrating that the spatial heterogeneity of K^+ channels is an important characteristic of axons.[15,40,47,48] Furthermore, the conduction failure rate modulated by heterogeneity, K^+ conductance, stimulation frequency, and coupling current is investigated through bifurcation analysis and current-threshold calculations. Conduction failure occurs in isolated compartments/nodes and multiple consecutive compartments/nodes with large K^+ conductance owing to their high current thresholds. The larger the degree of heterogeneity, the higher the conduction failure rate, and the more compartments/nodes exhibit an increasing conduction failure rate with conduction distance. In addition, higher stimulation frequencies, weaker coupling currents, and larger K^+ conductances induce higher conduction failure rates. Moreover, the increasing conduction failure rate is further explained by the low membrane potential and weak coupling current in compartments with high K^+ conductance. The results closely match experimental observations,[12,13,15] and are helpful for understanding irregular firing patterns and the increasing conduction failure rate along axons, while providing potential measures for modulating conduction failure.

2. Models and methods

2.1. The axonal model with spatial heterogeneity of ion channel

In the present paper, the axon is described as a network containing many nodes (also called compartments), which are connected by electrical coupling. Different values of K^+ conductance are considered for different nodes to represent heterogeneity. The network model with spatial heterogeneity is as follows:

$$\begin{cases} C\dfrac{\mathrm{d}V_i}{\mathrm{d}t} = I_{\mathrm{Na},i} + I_{\mathrm{K},i} + I_{\mathrm{L},i} + I_{\mathrm{app},i} + I_{\mathrm{cou},i}, \\ \dfrac{\mathrm{d}x_i}{\mathrm{d}t} = \alpha_x(V_i) - (\alpha_x(V_i) + \beta_x(V_i))\, x_i, \end{cases} \tag{1}$$

where the subscript i represents the node number, as shown in Fig. 1(a). C is the membrane capacitance. V_i denotes the membrane potential of node i. In the second equation of Eq. (1), x_i represents the gating variables of the Na^+ and K^+ channels of node i, namely m_i, h_i, and n_i. In the present paper, $i = 1$ to N ($N = 100$). The five terms on the right-hand side of the first equation in Eq. (1) represent the Na^+, K^+, leakage, applied, and coupling currents, respectively.

The three ionic currents are described as follows: $I_{\mathrm{Na},i} = -g_{\mathrm{Na}} m_i^3 h_i (V_i - E_{\mathrm{Na}})$, $I_{\mathrm{K},i} = -g_{\mathrm{K},i} n_i^4 (V_i - E_{\mathrm{K}})$, and $I_{\mathrm{L},i} = -g_{\mathrm{L}} (V_i - E_{\mathrm{L}})$. Here, g_{Na}, $g_{\mathrm{K},i}$, and g_{L} denote the maximal conductances, while E_{Na}, E_{K}, and E_{L} are the reversal potentials. In particular, the values of $g_{\mathrm{K},i}$ vary with i, which are used to characterize the heterogeneous distribution of potassium channels along the axon.

At both ends of the axonal chain model, a node ($i = 1$ or 100) is coupled to only one adjacent node. Therefore, the coupling currents are $I_{\text{cou},1} = -g_{\text{c}}(V_1 - V_2)$ and $I_{\text{cou},100} = -g_{\text{c}}(V_{100} - V_{99})$, where g_{c} is the coupling strength. For other values of i, $I_{\text{cou},i}$ is given by $g_{\text{c}}(V_{i-1} - 2V_i + V_{i+1})$.

The α_x and β_x in the second equation of Eq. (1) are dependent on V_i and are given as follows:

$$\alpha_m(V_i) = \frac{0.1(25 - V_i)}{\exp\left(\frac{25 - V_i}{10}\right) - 1}, \quad \beta_m(V_i) = 4\exp\left(-\frac{V_i}{18}\right),$$

$$\alpha_h(V_i) = 0.07\exp\left(-\frac{V_i}{20}\right),$$

$$\beta_h(V_i) = \frac{1}{\exp((30 - V_i)/10) + 1},$$

$$\alpha_n(V_i) = \frac{0.01(10 - V_i)}{\exp((10 - V_i)/10) - 1},$$

$$\beta_n(V_i) = 0.125\exp\left(-\frac{V_i}{80}\right).$$

The parameter values and units are listed in Table 1.

Table 1. Parameters of model.

Parameter	C	$I_{\text{app},i}$	E_{Na}	E_{K}	E_{L}	g_{Na}	g_{L}
Unit	μF/cm^2	μA/cm^2	mV	mV	mV	mS/cm^2	mS/cm^2
Value	1	6.2	115	12	10.599	120	0.3

2.2. Conduction failure rate

To be consistent with experiments,[12] action potentials/spikes are induced at one end of the axon ($i = 1$–5, referred to as the stimulation region) in this study, as shown in Fig. 1(a). The nodes with $i = 6$–100 are referred to as the conduction region. The external voltage impulse stimuli applied to induce action potentials are shown in the top panel of Fig. 1(b). To ensure that a single stimulus induces a single action potential, the stimulus pulse is set to a width of 2 ms and an amplitude of 15 mV, while the period T_{s} is chosen as a control parameter. The action potentials of node 5 within the stimulation region are illustrated in the middle panel of Fig. 1(b), while those of node 6 within the conduction region are illustrated in the bottom panel.

Faithful conduction means that each action potential can propagate from the stimulation region to node i ($i = 6$ to 100). If only some action potentials can propagate, conduction failure occurs. Conduction block refers to the situation in which no action potentials can propagate to any node i within the conduction region. The degree of conduction failure is quantified by the conduction failure rate (denoted by R_i), which is defined as the ratio of the number of missed spikes to the number of stimulus pulses. For example, in Fig. 1(b), the number of stimulus pulses is 8, and 4 spikes are missed at node 6; therefore, $R_6 = 4/8 = 0.5$. $R_i = 0$ for nodes 6–100 and $R_i = 1$ for nodes 6–100 denote faithful conduction and conduction block, respectively. A value of $0 < R_i < 1$ for a node with $i = 6$–100 indicates conduction failure.

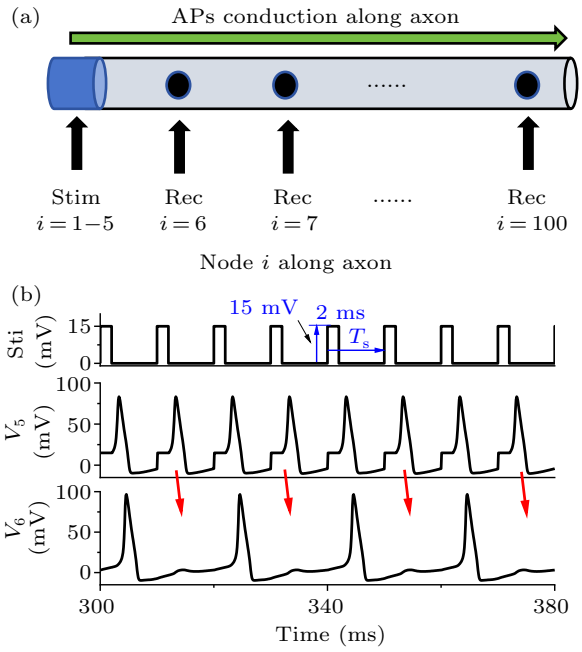


Fig. 1. (a) Schematic map of evoked spikes in the stimulation region and propagation of spikes along the axon; (b) Top: The external impulse stimulus (width: 2 ms, amplitude: 15 mV, and period T_{s}). Middle: The action potentials of node 5. Bottom: Conduction failure at node 6.

2.3. Spatial distribution of conductance of K^+ channel

In this study, the conductance of K^+ channels in the conduction region, $g_{\text{K},i}$ ($i = 6$ to 100), is inhomogeneous. The values of $g_{\text{K},i}$ ($i = 6$ to 100) obey a uniform distribution, i.e., $g_{\text{K},i} = gK + \eta\xi_{m,i}$, where $\xi_{m,i}$ ($m = 1$ or 2) obeys a uniform distribution between -1 and 1, and gK and η are constants. Two realizations of $\xi_{m,i}$ ($m = 1$ and 2) are shown in Fig. 2, where $m = 1$ corresponds to Fig. 2(a) and $m = 2$ corresponds to Fig. 2(b). For both realizations, $\xi_{m,i} = 0$ from $i = 1$ to 5. When $m = 1$, from left to right, $\xi_{1,i}$ exhibits large $g_{\text{K},i}$ values at

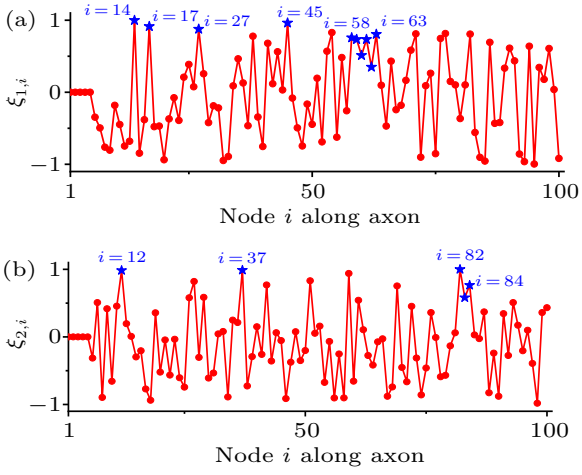


Fig. 2. Two realizations of the inhomogeneous K^+-channel conductance distribution for 100 nodes. (a) One realization. (b) Another realization different from panel (a).

$i = 14$, 17, 27, 45, and at several consecutive nodes from 58 to 63. After node 62, there are also some nodes with large values of $\xi_{1,i}$. When $m = 2$, from left to right, $\xi_{2,i}$ exhibits large $g_{\mathrm{K},i}$ values at $i = 12$ and 37, and at several consecutive nodes from 82 to 84. These large $g_{\mathrm{K},i}$ values play important roles in influencing conduction failure. In this paper, only the conduction behaviors under two random distributions of $g_{\mathrm{K},i}$ are presented. The results obtained under other random distributions are similar and are therefore omitted.

2.4. Methods

The equations in this paper are solved using the fourth-order Runge–Kutta method, and the integration time step is set to 0.001 ms. In this paper, gK, η, g_{c}, and T_{s} are treated as control parameters.

3. Results

3.1. The conduction dynamics change little for axon without heterogeneity

In this section, homogeneous conductance with $\eta = 0$ is considered, i.e., gK is fixed at 42.5 mS/cm^2, which is used as the control case for comparison with the heterogeneous case, i.e., $\eta > 0$.

3.1.1. Unchanged conduction failure rate

The action potentials at nodes $i = 3$, 8, 35, and 80 with $T_{\mathrm{s}} = 20$ ms are shown in Fig. 3(a1). Spikes with a time interval

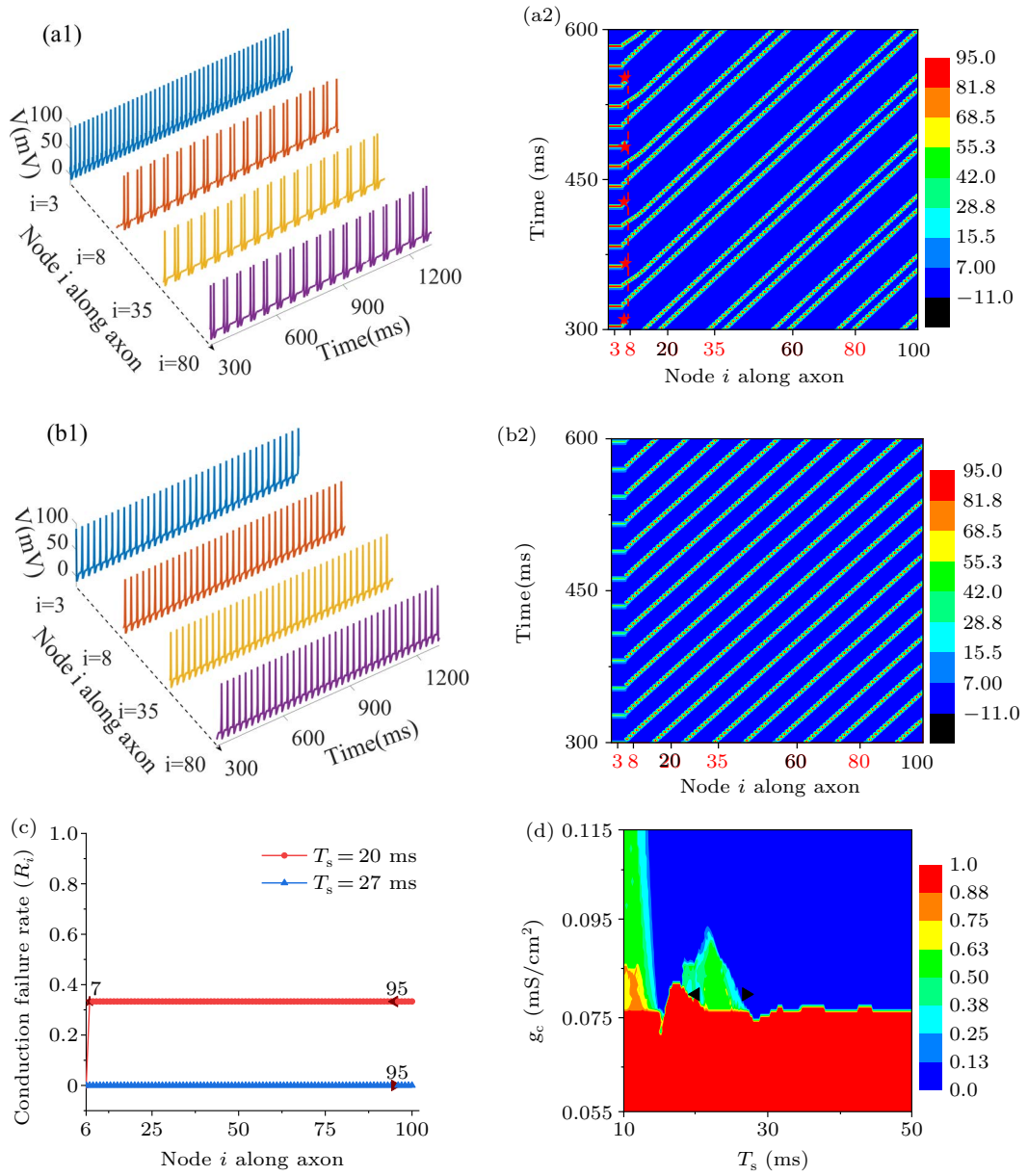


Fig. 3. Dynamics for an axon with homogeneous conductance ($\eta = 0$), with $gK = 42.5$ mS/cm^2 and $g_{\mathrm{c}} = 0.080$ mS/cm^2. Conduction failure for $T_{\mathrm{s}} = 20$ ms: (a1) Action potentials at nodes 3, 8, 35, and 80; (b1) Spatiotemporal dynamics for all nodes, where the membrane potential values are indicated by the color scale. Faithful conduction for $T_{\mathrm{s}} = 27$ ms: (a2) Action potentials at nodes 3, 8, 35, and 80; (b2) Spatiotemporal dynamics for all nodes. (c) The changes of R_i with respect to i for $T_{\mathrm{s}} = 20$ ms (red) and 27 ms (blue). (d) The distribution of R_i for node $i = 95$ in the plane (T_{s}, g_{c}).

of 20 ms appear at node 3 in the stimulation region. However, for nodes 8, 35, and 80 in the conduction region, one spike out of every three is missed, indicating the occurrence of conduction failure. The spatiotemporal dynamics of the 100 nodes between 300 ms and 600 ms are shown in Fig. 3(a2). The action potentials (spikes) are depicted by green/yellow/red lines. The horizontal part corresponds to the stimulation region ($i < 6$), and the part with a positive slope corresponds to the conduction region ($i = 6$ to 100). In the conduction region, one spike out of every three fails to propagate along the axon. R_i for $i = 7$ to 100 is $1/3$. The firing pattern is regular, i.e., one spike out of every three is missed. The conduction failure occurs only at node 7, as indicated by the stars in Fig. 3(a2). Then, R_i does not change within the conduction region, differing from the experimental observations.[12] The locations of nodes 3, 8, 35, and 80 are marked by red numbers on the coordinate axis in Fig. 3(a2).

As T_s increases to 27 ms, no spikes fail to propagate at nodes 8, 35, and 80, compared with node 3, as shown in Fig. 3(b1), indicating that conduction failure does not occur and faithful conduction is achieved. As shown in Fig. 3(b2), all spikes propagate along the axon, exhibiting a time interval of 27 ms. Then, R_i for $i = 6$ to 100 is equal to zero. The locations of nodes 3, 8, 35, and 80 are depicted by the red numbers on the coordinate axis in Fig. 3(b2).

The changes of R_i with respect to i ($i = 6$ to 100) are depicted in Fig. 3(c), red for $T_s = 20$ ms and blue for $T_s = 27$ ms. The results show that R_i, or the spiking pattern, does not change along the axon (from $i = 7$ to 100) for homogeneous conductance, regardless of whether conduction failure or faithful conduction occurs. In Figs. 3(a1), 3(a2), 3(b1), 3(b2), and 3(c), $g_c = 0.080$ mS/cm^2 and $gK = 42.5$ mS/cm^2.

3.1.2. The dependence of R_i for $i = 95$ on the plane (T_s, g_c)

As illustrated in Fig. 3(c), R_i ($i = 7$ to 100) for $T_s = 20$ ms and 27 ms does not change. Without loss of generality, R_i for node $i = 95$ at different T_s and g_c is calculated, as shown in Fig. 3(d). The blue region for $R_{95} = 0$ denotes faithful conduction, appearing for large g_c and long-to-intermediate T_s. For example, the black rightward triangle in Fig. 3(d) represents faithful conduction with $R_{95} = 0$, corresponding to the wine-colored rightward triangle in Fig. 3(c) for $T_s = 27$ ms. The red region corresponds to $R_{95} = 1$, i.e., no spikes propagate, which is called conduction block. Conduction block appears at small g_c. Other colored regions indicate $0 < R_{95} < 1$, i.e., conduction failure, appearing in two regimes: one is short T_s with large g_c, and the other is intermediate T_s with intermediate g_c. For example, the black leftward triangle in Fig. 3(d) represents $R_{95} = 1/3$, corresponding to the wine-colored leftward triangle in Fig. 3(c) for $T_s = 20$ ms. For other nodes in the conduction region, the distribution of R_i on the (T_s, g_c) plane is the same as in Fig. 3(d). However, when heterogeneous conductance is considered, the distribution of R_i on the (T_s, g_c) plane differs for different nodes.

3.1.3. Speculation on changes of R_i with respect to i for axon with heterogeneous conductance of K^+ channel

As reported in previous studies on homogeneous axons,[26,27] conduction failure occurs for large gK, since the resting membrane potential is lower, due to being farther from the Hopf bifurcation. It is then difficult for the coupling current to induce a spike from the lower membrane potential, characterized by an increased threshold for evoking a spike. Since these results can be used to speculate about the propagation dynamics along a heterogeneous axon, they are reproduced in Fig. 4. An isolated node (Eq. (1) with zero coupling current) exhibits a resting state (stable focus, solid dark yellow line), which changes to an unstable focus (red dotted line) with decreasing gK, via a Hopf bifurcation occurring at $gK_0 \approx 31.74$ mS/cm^2, as shown in Fig. 4(a). In addition, a fold bifurcation of limit cycles appears around 35.89 mS/cm^2, labeled as gK_1. For the resting state at 42.5 mS/cm^2 (labeled as gK_2) and 47.5 mS/cm^2 (labeled as gK_3), a positive perturbation can evoke an action potential, as illustrated in Fig. 4(b). The afterpotential following the evoked action potential is lower for larger gK. A pulsatile current resembling the coupling current is then applied to the damping afterpotentials, and the threshold current required to evoke a spike is calculated, as illustrated in Fig. 4(c). The threshold is higher for larger gK, as depicted in Fig. 4(d). The time coordinate in Fig. 4(d) corresponds to the period (T_s) of action potentials along the axon or the application time of the coupling current. Therefore, in this study, for a node with large $g_{K,i}$, it is difficult for a small coupling current to evoke a spike; consequently, conduction failure becomes more likely at this node.

For an axon with heterogeneous conductance ($\eta > 0$), the conduction of action potentials becomes difficult for nodes with large $g_{K,i}$, according to the results in Fig. 4. Then, the conduction failure rate R_i increases for nodes such as $i = 14$, 17, 27, 45, and 58–62, according to Fig. 2(a) ($m = 1$). For axons with heterogeneous conductance ($\eta > 0$), the distribution of R_i on the (T_s, g_c) plane for different nodes i changes with increasing i, which is consistent with experimental observations[12] and differs from the axon with homogeneous conductance (Fig. 3(d), $\eta = 0$). To ensure that the axon remains in the resting state, $g_{K,i} = gK + \eta\xi_{m,i}$ should be larger than the value at the fold bifurcation of limit cycles, appearing around $gK_1 \approx 35.89$ mS/cm^2. Considering $gK = 42.5$ mS/cm^2, $\eta < 6.6$ is required. The detailed results are addressed in the following subsection.

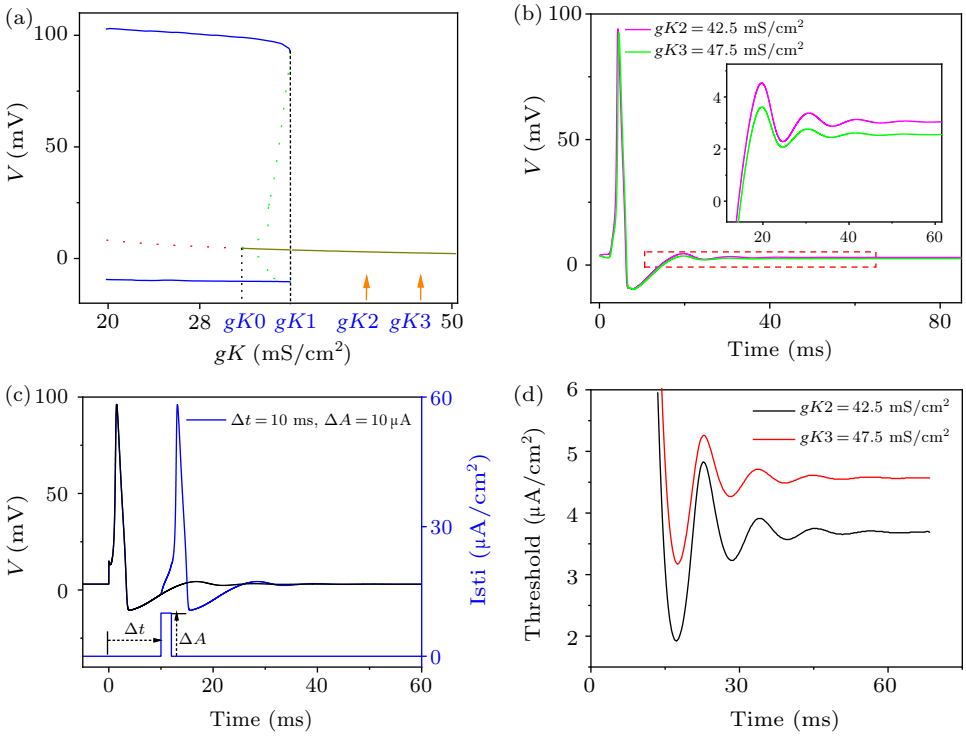


Fig. 4. Dynamics of the HH model for an isolated node. (a) Bifurcation with respect to gK. The red dotted line, the green dotted curve, and the solid dark yellow line represent the unstable focus, the amplitude of the unstable limit cycle, and the stable focus, respectively. The two blue solid curves in the upper and lower regions represent the amplitude of the stable limit cycle. (b) Lower afterpotential for larger gK_3 (green), compared with gK_2 (magenta). (c) A current pulse stimulation (width 2 ms and amplitude 10 μA) applied to the afterpotential (at $\Delta t = 10$ ms) can evoke a spike. (d) A larger threshold corresponds to larger gK.

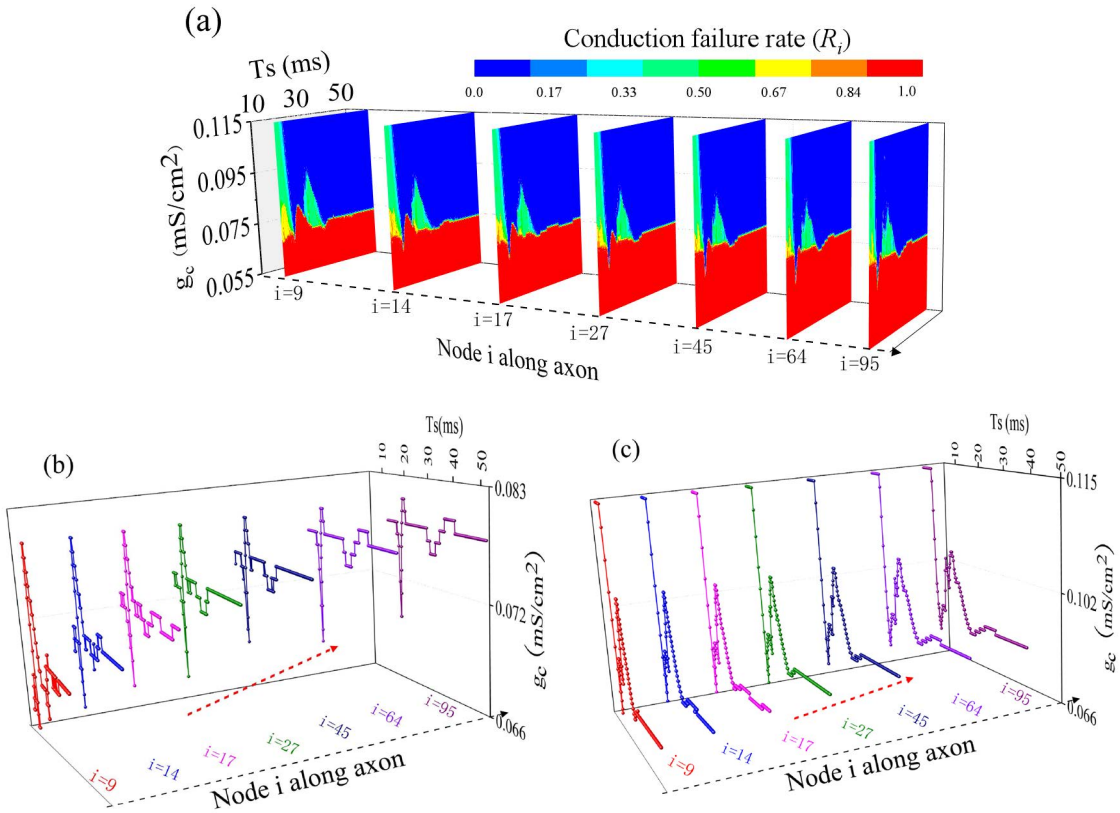


Fig. 5. Changes of R_i on the (T_s, g_c) plane with respect to i for $\eta = 1.8$ and $gK = gK_2$. (a) The distribution of R_i for nodes $i = 9$, 14, 17, 27, 45, 64, and 95. (b) The upper boundary of the conduction block shifts significantly upward. (c) The lower boundary of faithful conduction shifts upward for longer T_s.

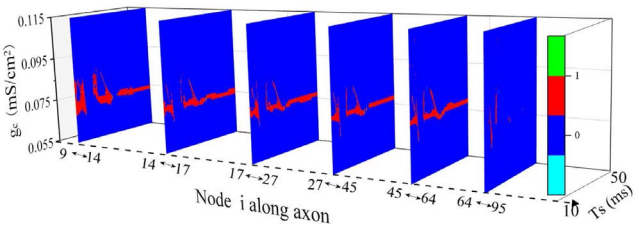


Fig. 6. The differences of R_i on the (T_s, g_c) plane between pairs of consecutive nodes (9 and 14, 14 and 17, 17 and 27, 27 and 45, 45 and 64, and 64 and 95) for $\eta = 1.8$ and $gK = gK_2$.

3.2. The complex conduction dynamics along axon with heterogeneous conductance

For $\eta > 0$, i.e., $g_{K,i} = gK + \eta\xi_{m,i}$ ($m = 1$ or 2), the conductance exhibits spatial heterogeneity. The conduction dynamics therefore change with respect to i. For instance, R_i increases around specific nodes with large $g_{K,i}$ values (such as $i = 14$, 17, 27, 45, and 58–62 when $m = 1$). The dependence of R_i and the spatiotemporal dynamics on η, T_s, g_c, and i is addressed in this subsection. First, the results for $m = 1$ are presented in Subsections 3.2.1–3.2.3, and then the results for $m = 2$ are presented in Subsection 3.2.4.

3.2.1. R_i on the (T_s, g_c) plane increases with respect to i

The distributions of R_i for nodes $i = 9$, 14, 17, 27, 45, 64, and 95 on the plane (T_s, g_c) are shown in Fig. 5(a). Clearly, the changes in the upper boundary of the conduction block (red region) with respect to i are shown in Fig. 5(b), exhibiting an increasing trend (red upward-sloping arrow). The lower boundary of the faithful conduction region (blue region) for different i is shown in Fig. 5(c), also exhibiting an increasing trend (red upward-sloping arrow). Both results indicate that the conduction failure region (non-red and non-blue region) shifts toward higher g_c as i increases. Therefore, R_i changes with respect to conduction distance (i), closely matching experimental observations[12] and supporting the speculation in Subsection 3.1.3. Here, $\eta = 1.8$ and $gK = gK_2$.

The detailed changes of R_i on the (T_s, g_c) plane between consecutive nodes for $i = 9$, 14, 17, 27, 45, 64, and 95 are shown in Fig. 6, where the values for smaller i are subtracted from those for larger i. On each panel, only positive values (red) and zero (blue) appear, indicating that R_i increases within the red region. The red region corresponds to the borders of the conduction failure region and the boundaries between the conduction block and faithful conduction regions.

3.2.2. Representatives for the irregular firing

As shown in Figs. 3(a1) and 3(a2), for $\eta = 0$ and $T_s = 20$ ms, R_i increases around node 7, which is regarded as the initial node of the conduction region. However, for $\eta = 1.8$ and $T_s = 20$ ms, R_i changes at two sites. One is around node 7, and the other is at nodes 58–61, indicated by the connected pentagram markers in Fig. 7(a2), corresponding to a large $g_{K,i}$. Compared to regular spiking with an interspike interval of 20 ms for node 3, the nodes 8, 61, and 80 in the conduction region exhibit irregular firings with long interspike intervals, i.e., conduction failure appears, similar to experimental observations.[12] R_i for node 61 increases significantly compared with node 8. However, R_i for node 80 changes little compared with that of node 61, as shown in Fig. 7(a1). The locations of nodes 3, 8, 61, and 80 are depicted by the red numbers on the x-coordinate in Fig. 7(a2). As T_s increases to 27 ms, R_i increases only around node 61, as shown in Figs. 7(b1) and 7(b2). Here, $gK = gK_2$, $\eta = 1.8$, and $g_c = 0.080$ mS/cm^2.

More detailed results for the changes of R_i with increasing i for $T_s = 20$ ms (red dotted marking line) and $T_s = 27$ ms (blue triangular marking line) are shown in Fig. 8(a). For long T_s, R_i increases only around nodes 61–64. For short T_s, R_i increases around nodes 7 and 61. R_i is higher for shorter T_s. As η increases, R_i increases, which is discussed in the following paragraphs.

3.2.3. R_i becomes higher for large η

As η increases to 2.5, i.e., the heterogeneity becomes stronger, the changes in R_i with increasing i for $T_s = 20$ ms (red dotted line) and 27 ms (blue triangular line) are shown in Fig. 8(b). Compared to $\eta = 1.8$, two changes are observed. One is that R_i increases around multiple nodes, such as $i = 28$, 45, and 60 for $T_s = 27$ ms and nodes 7, 14, 17, 27, and 60 for $T_s = 20$ ms. The other is that R_i becomes higher for larger η. For instance, the blue curve in the right panel is higher than that in the left panel, and the red curve shows the same trend. In particular, R_i for nodes with $i > 60$ increases to 1, indicating that conduction block occurs. All firing patterns associated with conduction failure in the left panels are irregular.

For $T_s = 20$ ms and $\eta = 2.5$, the firing patterns at nodes 3, 7, 14, and 30, and the resting state at node 80 are illustrated in Fig. 9(a1), and the spatiotemporal dynamics are illustrated in Fig. 9(a2). As i increases, the number of action potentials decreases gradually, indicating that R_i increases. As a consequence, R_i for $i = 7$ is 0.27, for $i = 14$ is 0.42, for $i = 30$ is 0.66, and for $i = 80$ is 1. For $T_s = 27$ ms, the results are depicted in Figs. 9(b1) and 9(b2). Similarly, R_i increases with increasing i. R_i for $i = 14$ is 0, for $i = 30$ is 0.2, for $i = 50$ is 0.4, and for $i = 80$ is 1. Additionally, for the same node i, R_i of conduction failure for $T_s = 27$ ms is smaller than that for $T_s = 20$ ms.

In order to investigate the influence of the heterogeneity degree of the axon on conduction dynamics, R_i along the conduction distance is calculated at six values of η ($\eta = 3.0$, 2.5, 2.0, 1.8, 1.5, and 1.0), at different T_s (20 ms, 27 ms, 40 ms, and 50 ms), with $gK = gK_2$ and $g_c = 0.080$ mS/cm^2, as shown in Fig. 10. The results for $T_s = 20$ ms are presented

in Fig. 10(a). For small η, such as 1.0 (red) and 1.5 (blue), R_i changes only around node 7, resembling that of $\eta = 0$ to a large extent. For $\eta = 1.8$ (magenta), in addition to node 7, R_i also changes around node 61 (Fig. 8). For $\eta = 2.0$ (olive), R_i increases at multiple nodes. In addition to nodes 7 and 62, R_i also increases around node 45. In particular, $R_i = 1$ appears for $i > 62$, meaning that no spikes can be conducted to nodes beyond $i = 63$. For $\eta = 2.5$ (navy), the nodes with enhanced R_i become more numerous, such as nodes 7, 14, 17, 27, and 60. Similarly, $R_i = 1$ appears for $i > 60$, meaning that no spikes can be conducted to nodes beyond $i = 61$. For $\eta = 3.0$ (violet), R_i increases around nodes 7, 14, 17, 27, and 45. No spikes can be conducted to nodes beyond $i = 45$, which shifts forward compared with node 61 for $\eta = 2.5$ and node 63 for $\eta = 2.0$. Furthermore, R_i for $i < 61$ increases compared with that for $\eta = 2.5$. In summary, for larger η, R_i increases at more nodes, and overall R_i becomes larger, leading to an enhanced conduction failure rate.

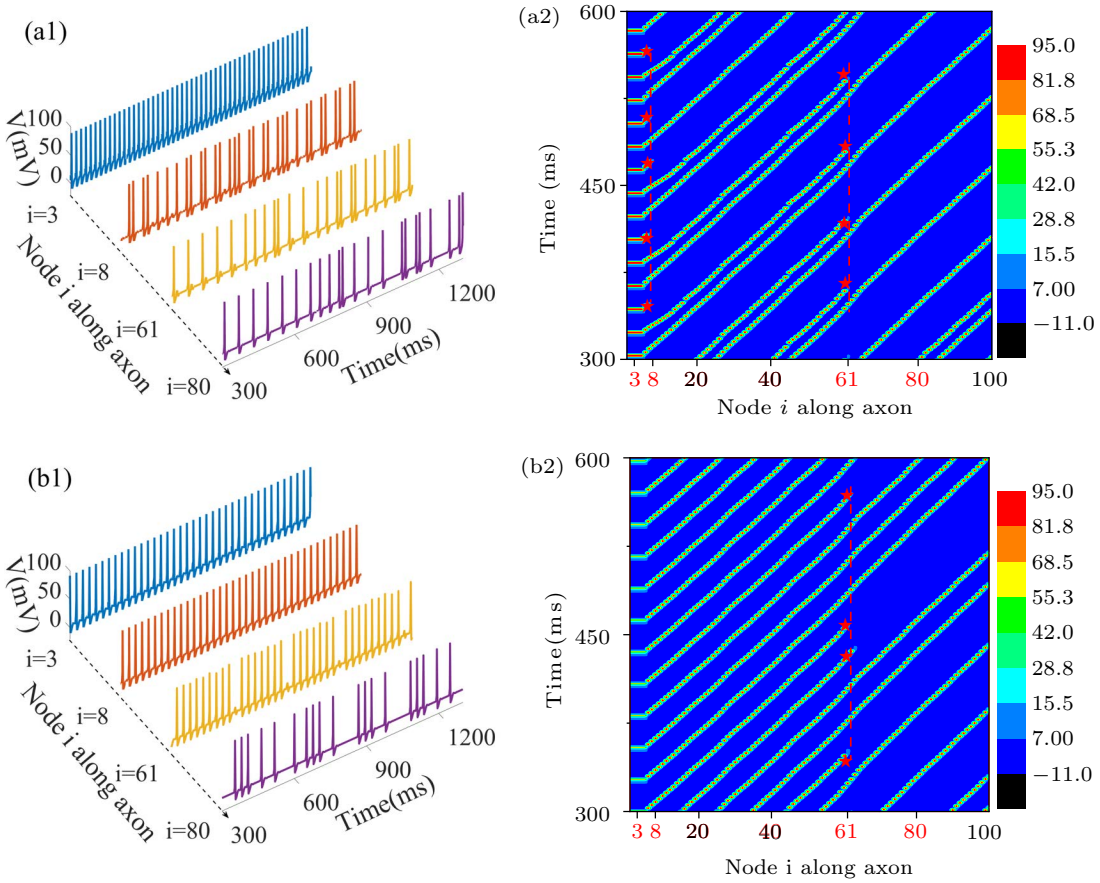


Fig. 7. Conduction failure dynamics of an axon with heterogeneous conductance ($\eta = 1.8$) for $T_s = 20$ ms (upper row) and $T_s = 27$ ms (lower row). (a1) and (b1) Action potentials at nodes 3, 8, 61, and 80; (a2) and (b2) Spatiotemporal dynamics for all nodes along the axon, where the membrane potential values are indicated by the color scale. $gK = gK_2$ and $g_c = 0.080$ mS/cm^2.

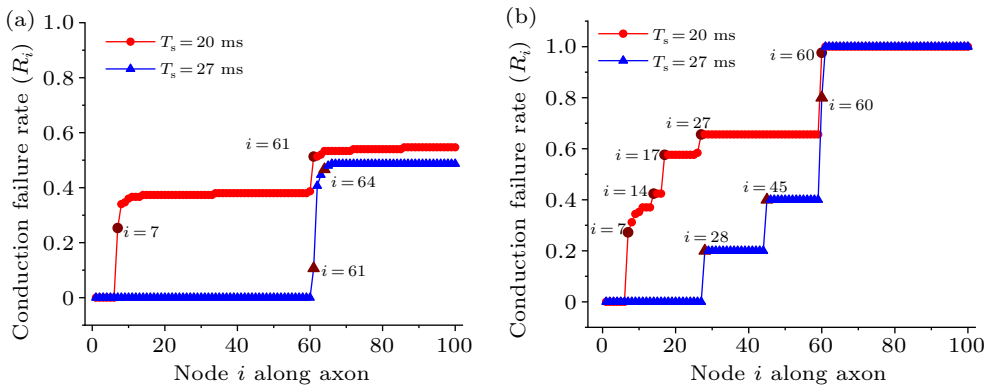


Fig. 8. The changes of R_i with respect to i for $T_s = 20$ ms (red dot marking line) and 27 ms (blue triangular marking line) at different η values. (a) $\eta = 1.8$; (b) $\eta = 2.5$. Here $gK = gK2$ and $g_c = 0.080$ mS/cm^2.

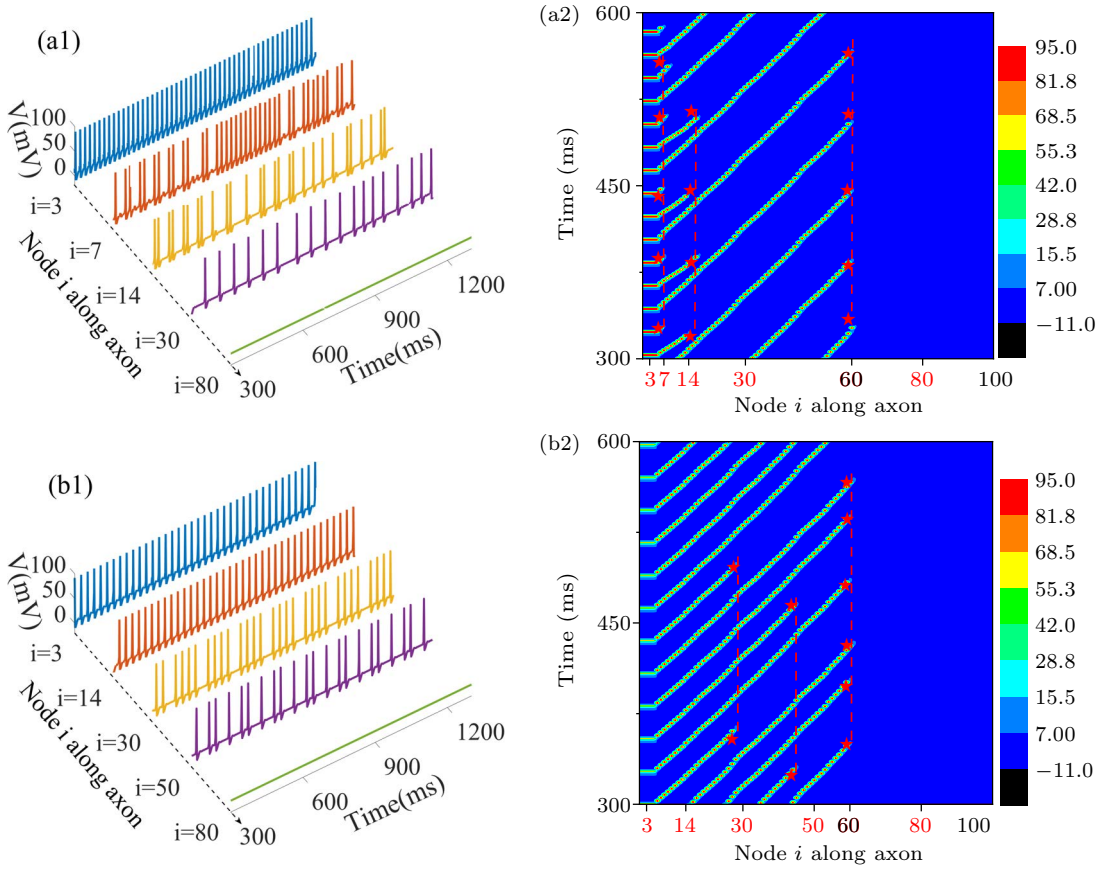


Fig. 9. Conduction failure dynamics of an axon with heterogeneous conductance ($\eta = 2.5$) for $T_s = 20$ ms (upper row) and $T_s = 27$ ms (lower row). (a1) Action potentials at nodes 3, 7, 14, 30, and 80; (b1) Action potentials at nodes 3, 14, 30, 50, and 80; (a2) and (b2) Spatiotemporal dynamics for all nodes along the axon, where the membrane potential values are indicated by the color scale. Here $gK = gK_2$ and $g_c = 0.080$ mS/cm^2.

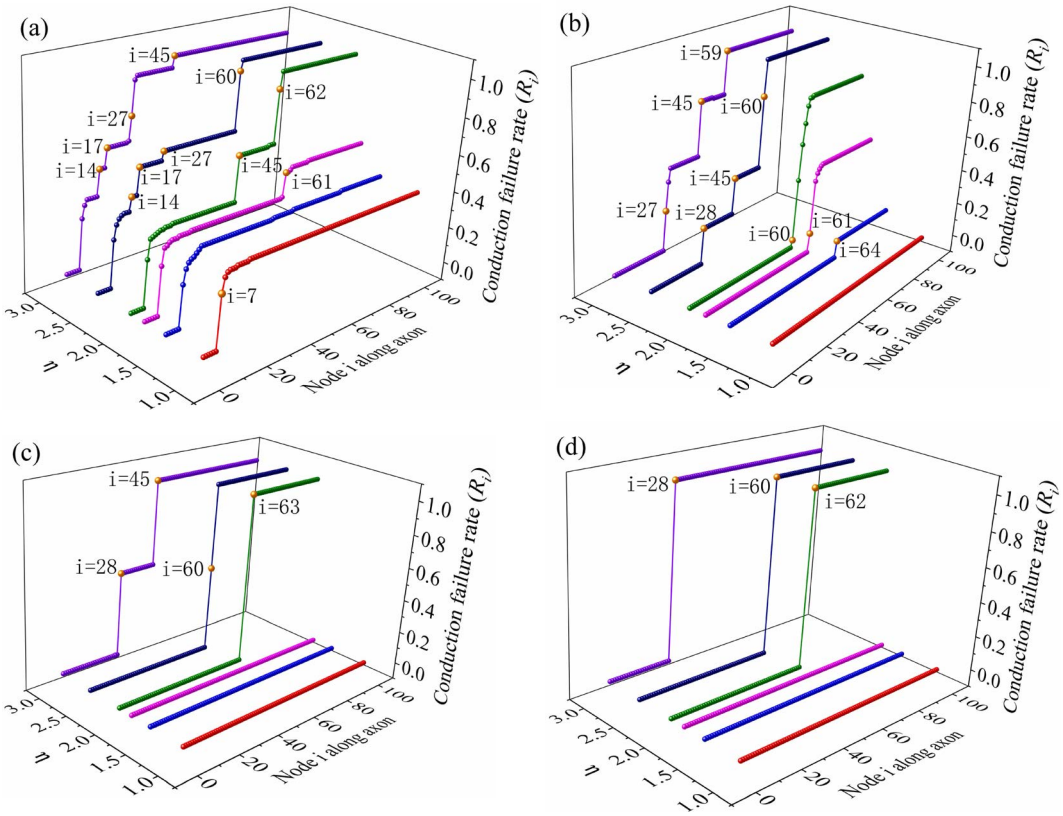


Fig. 10. Changes of R_i with respect to i at $\eta = 3.0$ (violet), 2.5 (navy), 2.0 (olive), 1.8 (magenta), 1.5 (blue), and 1.0 (red) for different T_s. (a) $T_s = 20$ ms; (b) $T_s = 27$ ms; (c) $T_s = 40$ ms; (d) $T_s = 50$ ms. gK and g_c are gK_2 and 0.080 mS/cm^2, respectively.

The results for $T_s = 27$ ms, 40 ms, and 50 ms are illustrated in Figs. 10(b)–10(d). Although Figs. 10(b)–10(d) exhibit similarity to Fig. 10(a) to a large extent, there are still some distinctions. The similarity is as follows: R_i increases at more nodes for larger η, and R_i is larger for more nodes, leading to an increased conduction failure rate. The distinction is as follows: the number of nodes with enhanced conduction failure decreases for longer T_s.

3.2.4. The conduction failure for $m = 2$ (Fig. 2(b))

When another random distribution is considered ($m = 2$, Fig. 2(b)), the results for $T_s = 20$ ms are presented in Fig. 11(a). For small η, such as 1.0 (red) and 1.5 (blue), R_i changes only around node 7. For $\eta = 1.8$ (magenta), in addition to node 7, R_i also changes around node 82. For $\eta = 2.0$ (olive), R_i increases at multiple nodes. In addition to node 6 and node 12, R_i also increases around node 37. For $\eta = 2.5$ (navy), the nodes with enhanced R_i become more numerous, such as nodes 6, 12, 37, and 84. In particular, $R_i = 1$ occurs for $i = 84$, meaning that no spikes can be conducted to nodes beyond $i = 84$. For $\eta = 3.0$ (violet), $R_i = 1$ occurs for $i > 6$, meaning that no spikes can be conducted to nodes beyond $i = 7$, which shifts forward compared with node 84 for $\eta = 2.5$. Furthermore, R_i for $i < 84$ increases compared with that for $\eta = 2.5$. Corresponding to Fig. 2(b), R_i increases around nodes 6, 7, 12, 37, and several consecutive nodes from 82 to 84 where $g_{K,i}$ has large values. For larger η, R_i increases at more nodes, and overall R_i becomes larger, leading to an increased conduction failure rate. The results for $T_s = 27$ ms, 40 ms, and 50 ms in Figs. 11(b)–11(d) are similar to those in Figs. 10(b)–10(d). These results indicate that the conduction failure dynamics are similar for different random distributions of the maximal conductance of potassium ion channels along the axon. To avoid repetition, the results for the random distribution with $m = 2$ are briefly presented, and other conclusions are similar to those for $m = 1$.

In addition, for the two trials of the random distribution of potassium conductance shown in Figs. 2(a) and 2(b), the conductance value for node 6 or 7 is not the largest. If it were the largest, the conduction failure rate for node 6 or 7 would become very high, and the phenomenon of increased conduction failure at multiple nodes would disappear, which is why relatively small potassium conductances for nodes 6 and 7 are used in this paper.

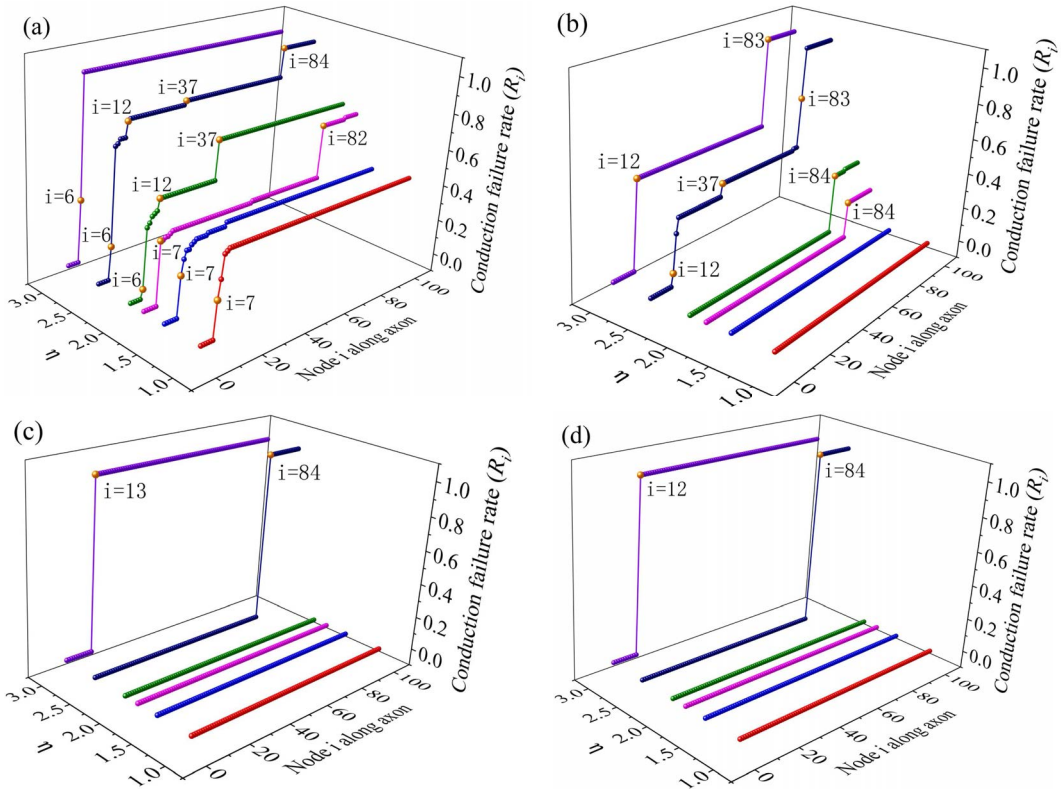


Fig. 11. For another random distribution ($m = 2$, Fig. 2(b)), the changes of R_i with respect to i at $\eta = 3.0$ (violet), 2.5 (navy), 2.0 (olive), 1.8 (magenta), 1.5 (blue), and 1.0 (red) for different T_s. (a) $T_s = 20$ ms; (b) $T_s = 27$ ms; (c) $T_s = 40$ ms; (d) $T_s = 50$ ms. gK and g_c are gK_2 and 0.080 mS/cm^2, respectively.

3.3. Simple indicators to characterize the change of R_i with respect to i

The current threshold shown in Fig. 4 can be used to characterize the conduction failure for an axon with $\eta = 0$. In the present paper, simple and feasible indicators to characterize conduction failure for an axon with $\eta > 0$ are presented, namely coupling current, total current, and membrane potential of a node i. If these three indicators have small values, the

node i is more likely to exhibit conduction failure.

3.4. Currents and V at a node i

For a node i, the dynamics of the membrane potential V_i modulated by currents is described as follows:

$$C\frac{\mathrm{d}V_i}{\mathrm{d}t} = I_{\mathrm{Na},i} + I_{\mathrm{K},i} + I_{\mathrm{L},i} + I_{\mathrm{app},i} + I_{\mathrm{cou},i} = I_{\mathrm{total},i} + I_{\mathrm{cou},i}, \quad (2)$$

(the first equation of Eq. (1)), where $I_{\mathrm{total},i} = I_{\mathrm{Na},i} + I_{\mathrm{K},i} + I_{\mathrm{L},i} + I_{\mathrm{app},i}$ denotes the total current, $I_{\mathrm{Na},i} = -g_{\mathrm{Na}} m_i^3 h_i (V_i - E_{\mathrm{Na}})$ represents the Na^+ current, and $I_{\mathrm{cou},i}$ denotes the coupling current. The node i in the conduction region receives a positive coupling current $I_{\mathrm{cou},i}$, and $I_{\mathrm{cou},i}$ and $I_{\mathrm{total},i}$ jointly modulate V_i. These indicators for node $i = 61$ are shown in Fig. 12, with $g_{\mathrm{c}} = 0.080$ mS/cm^2, $T_{\mathrm{s}} = 27$ ms, $gK = gK_2$, and $\eta = 1.8$. For node 61, the first row represents $I_{\mathrm{cou},61}$ and the last row represents V_{61}. As shown in the last row, the first spike fails to conduct, while the next two spikes conduct. As depicted in the first row, a positive peak of $I_{\mathrm{cou},61}$ is evoked by the spike at node 60, as indicated by the red, blue, and blue arrows. The positive peak of $I_{\mathrm{cou},61}$ following the action potential at node 61 is ignored, since it is induced by the spike of node 62.

For node 61, if the peak of $I_{\mathrm{cou},i}$ at a certain moment is strong enough to elevate V_i so that the Na^+ current ($I_{\mathrm{Na},i} = -g_{\mathrm{Na}} m_i^3 h_i (V_i - E_{\mathrm{Na}})$) rises rapidly, then $I_{\mathrm{total},i}$ becomes sufficient to trigger an action potential. Consequently, a spike is evoked when $I_{\mathrm{cou},i}$ and $I_{\mathrm{total},i}$ are large and V_i is high. Conversely, if $I_{\mathrm{cou},i}$ is too weak at a given moment, V_i remains low, $I_{\mathrm{total},i}$ is insufficient, and no spike is evoked, resulting in conduction failure. For instance, at the second peak indicated by a blue arrow in $I_{\mathrm{cou},i}$, $I_{\mathrm{cou},i} = 6.77$ μA/cm^2, $I_{\mathrm{total},i} = -1.668$ μA/cm^2, and $V_i = 5.413$ mV, the spike conducts. In contrast, at the peak indicated by a red arrow, $I_{\mathrm{cou},i} = 6.67$ μA/cm^2, $I_{\mathrm{total},i} = -1.785$ μA/cm^2, and $V_i = 5.286$ mV, the spike fails to conduct.

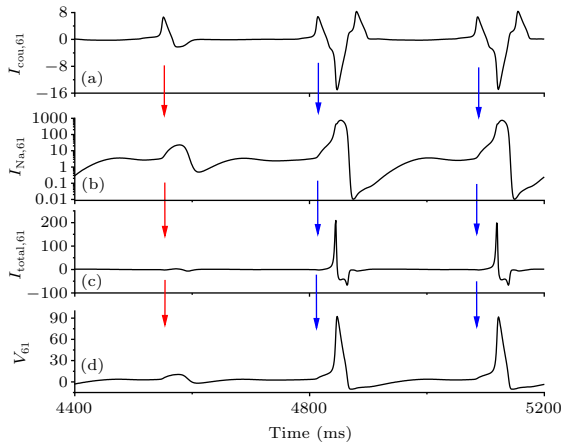


Fig. 12. Currents and membrane potential V of node $i = 61$ when conduction failure occurs, with $g_{\mathrm{c}} = 0.080$ mS/cm^2, $T_{\mathrm{s}} = 27$ ms, $gK = gK2$, and $\eta = 1.8$. (a) The coupling current at node 61 ($I_{\mathrm{cou},61}$); (b) The Na^+ current ($I_{\mathrm{Na},61}$); (c) The total current ($I_{\mathrm{total},61}$); (d) The membrane potential (V_{61}).

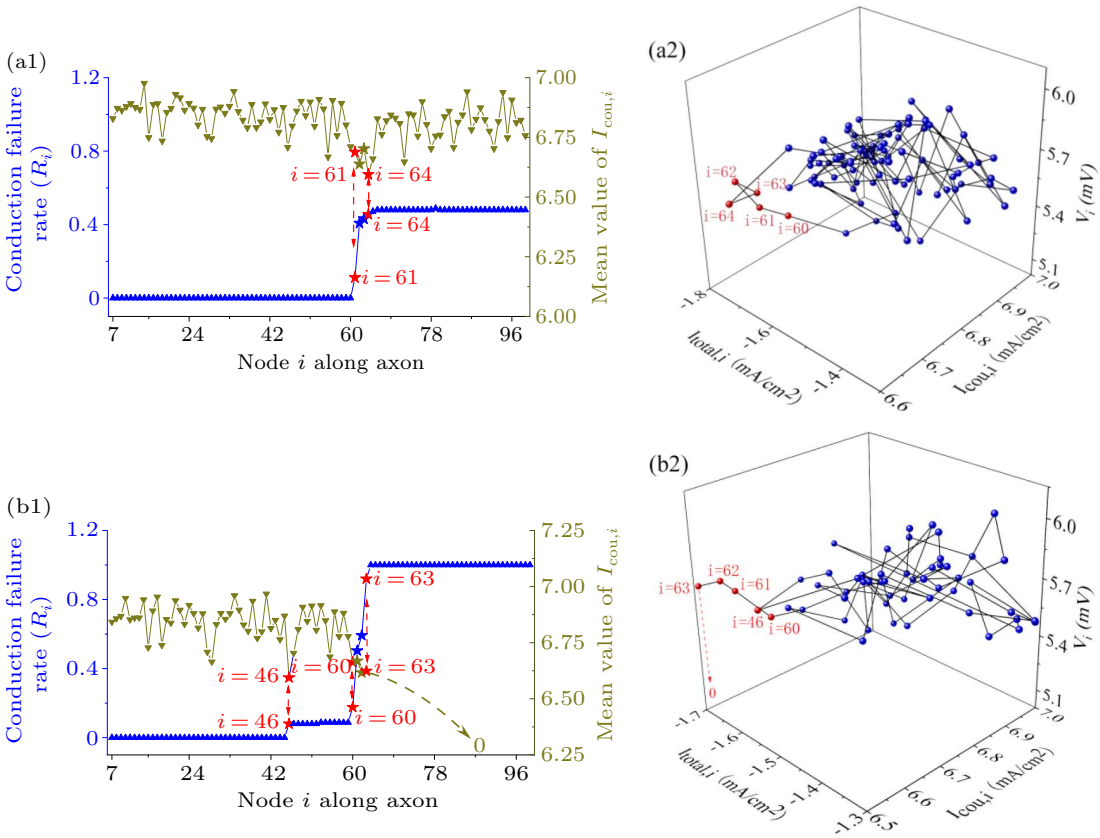


Fig. 13. Indicators to characterize conduction failure for $\eta = 1.8$ (upper row) and $\eta = 2.5$ (lower row) with $gK = gK2$, $g_{\mathrm{c}} = 0.08$ mS/cm^2, and $T_{\mathrm{s}} = 27$ ms. (a1) and (b1) Mean values of the coupling current (dark yellow down-triangular marking line) and R_i (blue up-triangular marking line) for nodes 7–99. (a2) and (b2) Mean values in the 3D space $(I_{\mathrm{cou},i}, I_{\mathrm{total},i}, V_i)$ at the first peak of $I_{\mathrm{cou},i}$ for nodes 7–99.

3.5. Lower currents and V at special nodes with large $g_{K,i}$ as indicators of R_i changes

For nodes $i = 7$ to 99, the mean values of $I_{cou,i}$, $I_{total,i}$, and V_i at the peak of $I_{cou,i}$ are calculated and plotted in the 3D space $(I_{cou,i}, I_{total,i}, V_i)$, as shown in Fig. 13. For $g_c = 0.08$ mS/cm^2, $T_s = 27$ ms, $gK = gK2$, and $\eta = 1.8$, the R_i in the conduction region changes primarily around nodes $i = 61$–64, illustrated by the blue up-triangular marking line in Fig. 13(a1) (corresponding to the blue line in Fig. 8(a)). The mean $I_{cou,i}$ is weak around these nodes, as indicated by the dark yellow down-triangular marking line in Fig. 13(a1). Consequently, in the 3D space $(I_{cou,i}, I_{total,i}, V_i)$, nodes 61–64 exhibit low values (red), as shown in Fig. 13(a2). These lower values of $I_{cou,i}$, $I_{total,i}$, and V_i induce conduction failure.

As η increases to 2.15, R_i changes around node 46 and nodes 61–64, as shown in Fig. 13(b1). Beyond node 63, no spikes are conducted ($R_i = 1$). The mean $I_{cou,i}$ is weak around node 46 and nodes 61–64, as indicated by the dark yellow down-triangular marking line in Fig. 13(b1), and zero for nodes 65–99. In the 3D space $(I_{cou,i}, I_{total,i}, V_i)$, nodes around 46 and 61–64 exhibit low values (red), as shown in Fig. 13(b2). Thus, a lower $(I_{cou,i}, I_{total,i}, V_i)$ provides a simple and feasible indicator to characterize conduction failure.

4. Discussion and conclusion

Conduction of action potentials along unmyelinated C-fibers plays a key role in pain signaling.[12,27,49–51] Recently, the traditional view of faithful conduction has been challenged by many experimental observations, such as conduction failure, which is related to a variety of abnormal functions or diseases.[19–21,52] Conduction failure depends on many factors, such as axonal structural properties,[11,18] ion channel dysfunction,[18,27,34–42,53] neuronal microenvironment,[24,26,28–31,54–56] pathological or traumatic factors,[13–15] temperature,[28–30] and noise,[24,30] which together give rise to complex nonlinear spatiotemporal dynamics. Although conduction failure has been extensively studied,[24–27,34] experimental observations in two aspects have not been fully explained: one is the irregular firing pattern, and the other is the enhanced conduction failure rate along conduction distance.[12] In the present paper, these two experimental observations are reproduced and explained in a chain network with spatial heterogeneity, which is significant in the following aspects.

Firstly, the simulation results for a chain network with spatial heterogeneity in potassium conductance closely match experimental observations in two aspects: stochastic firing associated with conduction failure and an enhanced conduction failure rate along conduction distance.[12] These results differ from previous theoretical studies based on spatially homogeneous models, where regular firing patterns for conduction failure and unchanged conduction failure rates along the axon were obtained.[24,26,27] The results of the present paper and other recent studies[35,36,38–42,46] suggest that spatial heterogeneity is an important characteristic of axons. In future research, another on–off firing pattern for conduction failure should also be studied in axons with spatial heterogeneity.

Second, changes in conduction failure modulated by spatial heterogeneity and other factors are obtained. Enhancement of the conduction failure rate occurs at isolated compartments or continuous segments with large K^+ conductance. For large K^+ conductance, a stronger coupling current is required to induce a spike, which provides a mechanism for the enhanced conduction failure rate. The larger the degree of heterogeneity is, the higher the conduction failure rate becomes, and the more compartments exhibit enhanced conduction failure. These results provide a novel perspective on conduction failure in axons with spatial heterogeneity. In addition, consistent with previous studies,[26,27] higher stimulation frequency of action potentials and weaker coupling current lead to a higher conduction failure rate, whereas smaller K^+ conductance reduces the conduction failure rate. These results provide practical measures to modulate conduction failure.

Finally, an explanation for the enhanced conduction failure rate is presented based on Hopf bifurcation and the dynamical response of the afterpotential (i.e., the current threshold for action potential initiation). For a compartment with large conductance, in addition to a larger distance from the Hopf bifurcation and a higher current threshold, the membrane potential, coupling current, and total current are all reduced. Consequently, it is difficult to induce a spike, and conduction failure is more likely to occur. Compared to bifurcation analysis and current-threshold methods,[26,27,57] calculating the membrane potential, coupling current, and total current is more straightforward, providing simple and feasible measures to characterize conduction failure. In future research, mechanisms of conduction failure in axons with other types of bifurcations should be investigated.

In the present paper, heterogeneity in only K^+ channels is considered. In future work, spatial heterogeneity in other important factors affecting action potential conduction should be considered, such as Na^+ channels and axonal radius, to explain experimental phenomena associated with Na^+ channels[13,19,41,42,46] and other mechanisms.

Acknowledgment

This work was supported by the National Natural Science Foundation of China (Grant Nos. 12202147, 12162002, 12202146, and 12372063).

References

[1] Wang X, Yu Y, Han F and Wang Q 2023 *Nonlinear dyn.* **111** 10505
[2] Wang T, Li B, Liu Y, Xu R, Xu Y, Yang Y and Zhang L 2025 *Electron. Res. Arch.* **33** 2412
[3] Han F, Wang Q and Su J 2023 *Cogn. Neurodyn.* **17** 1117
[4] Hodgkin A L and Huxley A F 1952 *Biophys. J.* **117** 500
[5] Hille B 2025 *Mol. Pharmacol.* **107** 100012
[6] Bucher D and Goaillard J M 2011 *Prog. Neurobiol.* **94** 307
[7] Xu J, Xu S, Wang F and Xu S 2021 *Chin. Phys. B* **30** 028701
[8] Zhai Q, Ooi K J A, Xu S and Ong C K 2022 *Chin. Phys. B* **31** 038701
[9] Sasaki T, Matsuki N and Ikegaya Y 2011 *Science* **331** 599
[10] Rama S, Zbili M and Debanne D 2018 *Curr. Opin. Neurobiol.* **51** 37
[11] Zang Y and Marder E 2021 *Proc. Nat. Acad. Sci.* **118** e2105795118
[12] Zhu Z R, Tang X W, Wang W T, Ren W, Xing J L, Zhang J R, Duan J H, Wang Y Y, Jiao X and Hu S J 2009 *Neurosignals* **17** 181
[13] Sun W, Miao B, Wang X C, Duan J H, Wang W T, Kuang F, Xie R G, Xing J L, Xu H, Song X J, Luo C and Hu S J 2012 *Brain* **135** 359
[14] Wang X C, Wang S, Wang W T, Duan J H, Zhang M, Lv X H, Niu C X, Tan C, Wu Y B, Yang J, Hu S J and Xing J L 2016 *Pain* **157** 2235
[15] Wang X C, Wang S, Zhang M, Gao F, Yin C, Li H, Zhang Y, Hu S J and Duan J H 2016 *J. Neurophysiol.* **115** 947
[16] Zhang Y C, Yang D H, Fan D K, Wang H T, Chen Y and Chen Y 2024 *Chaos* **34** 103132
[17] Song X, Wang H, Chen Y and Lai Y C 2019 *Phys. Rev. E* **100** 032416
[18] Wimmer V C, Reid C A, So E Y, Berkovic S F and Petrou S 2010 *J. Physiol.* **588** 1829
[19] Waxman S G 2006 *Nat. Rev. Neurosci.* **7** 932
[20] Leung G, Sun W, Brookes S, Smith D and Shi R 2011 *Exp. Neurol.* **227** 232
[21] Lesnick T G, Papapetropoulos S, Mash D C, Ffrench-Mullen J, Shehadeh L, de Andrade M, Henley J R, Rocca W A, Ahlskog J E and Maraganore D M 2007 *PLoS Genet.* **3** e98
[22] Yin H W, Yang S T, Wen X Q, Wang H H and Yang S F 2024 *Chin. Phys. B* **33** 110202
[23] Guo S L, Wang C N, Ma J and Jin W Y 2016 *Neurocomputing* **216** 627
[24] Zhang X J, Gu H G and Guan L N 2019 *Sci. China Tech. Sci.* **62** 1502
[25] Ma J, Song X L, Tang J and Wang C 2015 *Neurocomputing* **167** 378
[26] Zhang X J and Gu H G 2019 *Int. J. Bifurcation Chaos* **29** 1950093
[27] Zhang X J, Gu H G and Ma K H 2020 *Neurocomputing* **387** 293
[28] Tai C, Wang J, Roppolo J R and de Groat W C 2009 *J. Comput. Neurosci.* **26** 331
[29] Ganguly M, Jenkins M W, Chiel H J, Jansen E D 2016 *Proc. SPIE* **9690** 96901O
[30] Dai S, Lu L, Wei Z, Zhu Y and Yi M 2022 *Chaos, Solitons Fractals* **164** 112762
[31] Tai C, de Groat W C and Roppolo J R 2005 *IEEE Trans. Biomed. Eng.* **52** 1323
[32] Feng Z, Wang Z, Guo Z, Zhou W, Cai Z and Durand D M 2017 *Brain Res.* **1661** 67
[33] Li Z J, Xie W Q, Zeng J F and Zeng Y C 2023 *Chin. Phys. B* **32** 010503
[34] Lu M L, Gu H G and Zhang X J 2024 *Cogn. Neurodyn.* **18** 2433
[35] Waxman S G and Foster R E 1980 *Brain Res.* **2** 205
[36] Kaplan M R, Cho M H, Ullian E M, Isom L L, Levinson S R and Barres B A 2001 *Neuron* **30** 105
[37] Trimmer J S and Rhodes K J 2004 *Annu. Rev. Physiol.* **66** 477
[38] Hill A S, Nishino A, Nakajo K, Zhang G, Fineman J R, Selzer M E, Okamura Y and Cooper E C 2008 *PLoS Genet.* **4** e100317
[39] Zeng S and Tang Y 2009 *Phys. Rev. E* **80** 021917
[40] Rasband M N 2010 *Neurosci. Lett.* **486** 101
[41] Freeman S A, Desmazi'eres A, Fricker D, Lubetzki C and Sol-Foulon N 2015 *Cell. Mol. Life Sci.* **73** 723
[42] Johnston W L, Dyer J R, Castellucci V F and Dunn R J 1996 *J. Neurosci.* **16** 1730
[43] Mathis C, Denisenko-Nehrbass N, Girault J A and Borrelli E 2001 *Development* **128** 4881
[44] Desmazieres A, Zonta B, Zhang A, Wu L-M N, Sherman D L and Brophy P J 2014 *J. Neurosci.* **34** 5083
[45] Henry M A, Luo S and Levinson S R 2012 *BMC Neurosci.* **13** 29
[46] Zang Y, Marder E and Marom S 2023 *Curr. Biol.* **33** 1818
[47] Misonou H 2010 *Neuroscientist* **16** 51
[48] Rowan M J, DelCanto G, Yu J J, Kamasawa N and Christie J M 2016 *Neuron* **91** 370
[49] Orstavik K, Weidner C, Schmidt R, Schmelz M, Hilliges M, J'urum E, Handwerker H and Torebjork E 2003 *Brain* **126** 567
[50] Colloca L, Ludman T, Bouhassira D, Baron R, Dickenson A H, Yarnitsky D, Freeman R, Truini A, Attal N, Finnerup N B, Eccleston C, Kalso E, Bennett D L, Dworkin R H and Raja S N 2017 *Nat. Rev. Dis. Primers* **3** 17002
[51] Van Beek M, Van Kleef M, Linderoth B, Van Kuijk S M J, Honig W M and Joosten E A 2017 *Eur. J. Pain* **21** 795
[52] Yang C, Liu Z, Wang Q, Luan G and Zhai F 2020 *Cogn. Neurodyn.* **15** 43
[53] Shi R and Sun W 2011 *Neurosci. Bull.* **27** 36
[54] Zheng F, Lammert K, Nixdorf-Bergweiler B E, Steigerwald F, Volkmann J and Alzheimer C 2011 *J. Physiol.* **589** 2781
[55] Cross K P and Robertson R M 2016 *Physiol. Rep.* **4** e12814
[56] Zhong Y, Wang J, Beckel J, de Groat W C and Tai C 2021 *J. Comput. Neurosci.* **50** 203
[57] Zhang X J, Gu H G and Wu F Q 2019 *Eur. Phys. J. Special Topics* **228** 2053